

Fixed-mesh curvature-parameterized shape optimization of an acoustic horn

Fotios Kasolis · Eddie Wadbro · Martin Berggren

Abstract We suggest a boundary shape optimization approach in which the optimization is carried out on the coefficients in a boundary parameterization based on a local, discrete curvature. A fixed mesh is used to numerically solve the governing equations, in which the geometry is represented through inhomogeneous coefficients, similarly as done in the material distribution approach to topology optimization. The method is applied to the optimization of an acoustic horn in two space dimensions. Numerical experiments show that this method can calculate the horn's transmission properties as accurately as a traditional, body-fitted approach. Moreover, the use of a fixed mesh allows the optimization to create shapes that would be difficult to handle with a traditional approach that uses deformations of a body-fitted mesh. The parameterization inherently promotes smooth designs without unduly restriction of the design flexibility. The optimized, smooth horns consistently show favorable transmission properties.

Keywords shape optimization, material distribution approach, acoustic horns, Helmholtz equation

1 Introduction

Boundary shape optimization is a powerful technique, particularly useful for the final engineering design of components subject to, for instance, mechanical or electromagnetic performance requirements [15, 17, 22, 25]. Gradient-based boundary shape optimization, which is what we consider here, typically relies on a calculus of variation with respect to a set of parameters that governs displacements of the boundary with respect to a given reference domain.

Department of Computing Science, Umeå University, SE-901 87 Umeå, Sweden. E-mail: {fotios.kasolis · eddie.wadbro · martin.berggren}@cs.umu.se

We now discuss principles that we believe are important when constructing such a parameterization.

Unwise parameterization choices may cause the optimization algorithm to produce oscillatory or otherwise ragged shapes. For instance, disastrous results is usually obtained when individual displacements of the mesh vertices at the boundary are directly used as design variables, as demonstrated by Bängtsson et al. [3, Figs. 9, 12] for an acoustics problem of the type considered in this article, Haftka & Grandhi [16, Fig. 2] for a problem from linear elasticity, and Mohammadi & Pironneau [25, Fig. 5.1] for an airfoil optimization problem. One reason for the appearance of ragged shapes is that some locations on the design boundary are typically much more sensitive to local boundary displacements than others. Such differences in sensitivity tend to initiate ragged designs, if individual mesh vertex displacements are used as design variables. This problem can be seen in two of the examples mentioned above, Bängtsson et al. [3, Figs. 9, 12], and Mohammadi & Pironneau [25, Fig. 5.1].

Another cause of ragged shapes is the often low sensitivity for oscillatory perturbations of the design boundary in many physically relevant objective functions. That is, the difference in objective function values can be very small between a smooth shape and one containing oscillatory perturbations on the mesh-point level. The low sensitivity means that the optimization algorithm may not flatten out oscillatory shapes that may appear in intermediate design steps. The example by Haftka & Grandhi [16, Fig. 2] demonstrates the appearance of such wavy shapes.

A common approach to tackle the problem of ragged or oscillatory boundary shapes is to prevent them by drastically reducing the number of design variables and optimize over, say a handful of control points in a spline representation of the boundary. Although this approach may be useful in some cases, it somewhat defies the purpose of numerical boundary shape optimization; searching through a design

space spanned by a handful of design variables may as well be done manually by trial and error, and unexpected but successful shapes can easily be missed.

Another way to address the problem of ragged boundary shapes, and a better one in our opinion, is through a smoothing strategy [20], [25, § 5.2]. In this approach, the boundary displacements are indirectly specified through the solution of an elliptic differential equation, whose forcing term is the actual design variables. This strategy was used in the previous horn-optimization studies mentioned above [3, 28, 34].

A different viewpoint to the issue of ragged boundary shapes is to consider the *metric* that is provided, or implicitly assumed, in the optimization problem. The idea behind gradient-based optimization algorithms is to progress through a sequence of *small* parameter changes, using *local* approximations, typically linear or quadratic, of the objective function and constraints. The qualifiers “small” and “local” indicate the intrinsic reliance on a metric. The metric used in practical implementations of standard optimization algorithms is almost always derived from the norm associated with the dot product of the parameters. Assume now that the design variables are individual displacements of all the boundary mesh nodes. A small-amplitude oscillatory perturbation of the boundary constitutes a small design perturbation in the metric deduced from the sum-of-squares of the displacements. However, if instead the fundamental design variables are related to a local curvature, then a small perturbation of the design variables will necessarily correspond to small changes in curvature and hence smooth updates in the design. Such a choice of design variables does not explicitly prevent oscillatory shapes if the design space is large enough, but more iterations will be required to reach ragged designs compared to smooth ones, and the algorithm will be less prone to be caught in local minima associated with ragged shapes. In this article, we will use this idea in the context of optimizing the flare shape of an axially symmetric acoustic horn. We choose as design variables the angles between successive segments of constant length. Each such angle divided by the segment length constitutes a discrete curvature measure. The design smoothing strategy mentioned in the previous paragraph can be viewed as such a change of metric [3, § 3.2].

We use a finite-element discretization of the Helmholtz equation to model sound propagation in the acoustic horn. An issue that then has to be addressed is how to represent changes in the computational domain as the design boundary is changed. There are basically two options. Either we adapt the mesh to changes in the geometry, or we fix the mesh and represent the geometry through changing coefficients in the equation. The first option is perhaps the most common approach for boundary shape optimization. The computational mesh is then regenerated or deformed

at each design cycle in order to prevent the occurrence of invalid meshes when the boundary shape is modified. **A regeneration of the mesh is perhaps the easiest to implement, but a drawback is that the objective function and its gradient are mesh dependant. Thus, the regeneration creates “numerical noise” [21] that may interfere with the optimization algorithm.** Such effects can be avoided by using a mesh deformation algorithm [25, Ch. 5]. Moreover, by using mesh deformations, it is possible to calculate completely consistent derivatives, that is, derivatives of the *discrete* objective function that are exact up to roundoff. The price to pay for the consistency is the inclusion of “mesh sensitivities”, that is the Jacobian mapping of the mesh deformation algorithm, in the evaluation of derivatives. **The computation of such consistent derivatives leads to a chain of software dependencies between the different parts in the implementation.**

The second option, to keep the mesh fixed and represent geometry changes through an inhomogeneous coefficient in the governing equations, is the one we employ here. This is the same method to represent geometries as used in the material distribution method for topology optimization [4]. This varying-coefficient approach is most commonly used to enforce so-called natural boundary conditions at material interfaces; typical examples are traction-free boundaries of elastic media or, as here, sound-hard boundaries in acoustics. The fixed mesh simplifies the implementation and makes the method robust also for large displacements, and completely consistent derivatives are straightforward to compute. The price for the generality and the relative simplicity of the method is the fine meshes that are needed for a detailed geometry resolution and an unavoidable staircasing effect at the design boundaries. For the rather long wavelengths typical in the context of acoustic horns, such staircasing is however not so problematic.

The idea of mapping an explicit boundary representation to a material distribution parameter was exploited by Norato et al. [27] for the minimum-compliance design problem of elastic structures, and later for optics applications by Frei et al. [12–14]. The method is here tested on an acoustical shape-optimization problem that previously was addressed with traditional body-fitted meshes together with a mesh deformation approach [3, 28, 34].

Instead of relying on an explicit geometry model for the boundary, as we do here, several researchers instead use implicit representations through level sets; the boundary is assumed at the zeros of a scalar function, the level-set surface. This method also allows certain topological changes, such as the merging of unconnected regions. The level set surface can either be constructed as a parameterized function, whose parameters are subject to optimization [12–14, 23, 24], or the level set surface itself can be transported through a Hamilton–Jacobi equation that constitutes a con-

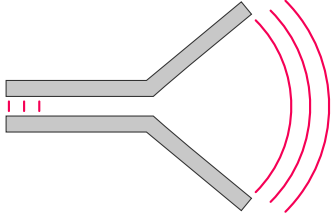


Fig. 1 The setup for the acoustic wave propagation problem.

tinuous analogue to the steepest-descent optimization algorithm [1, 2, 8, 36].

Examples of other approaches that have been suggested in order to utilize fixed meshes for shape optimization are the Extended Finite Element Method (X-FEM) [10, 24], a method developed to resolve nonsmooth solution features inside elements, and the element-free Galerkin method [5].

2 Problem statement

We consider the symmetric acoustic device, illustrated in figure 1, consisting of a horn with a semi-infinite waveguide attached to its left end. The device extends infinitely in the direction normal to the plane and consists of sound-hard walls. We assume that for the frequencies under consideration, all non-planar modes are geometrically evanescent in the waveguide. Within the waveguide, we consider a right-going monochromatic planar wave of frequency f and amplitude A . When the wave reaches the horn, some portion of its energy is reflected back yielding a left-going wave.

Under the assumption of time harmonic waves, the acoustic pressure P can be separated as $P(\mathbf{x}, t) = \Re(u(\mathbf{x})e^{i\omega t})$ and the wave equation

$$\frac{\partial^2 P}{\partial t^2} = c^2 \Delta P \quad (1)$$

reduces to the monochromatic steady-state Helmholtz equation

$$\Delta u + k^2 u = 0, \quad (2)$$

where $k = \omega/c$ is the wave number, $\omega = 2\pi f$ is the angular frequency, c is the phase velocity, u is the complex-valued acoustic pressure, and $\Delta = \nabla \cdot \nabla$ denotes the Laplacian.

For the purpose of computing, we truncate the infinite domain and we enforce its non-echoic character with a perfectly matched layer (PML) [19]. We consider only devices exhibiting mirror symmetry across a plane through the centerline of the waveguide. We may thus restrict the computation to the domain shown in figure 2.

Let Ω be the computational domain and let Γ_{in} denote the left boundary of the truncated waveguide (figure 2). We

impose the radiation condition

$$iku + \frac{\partial u}{\partial n} = 2ikA \quad \text{on } \Gamma_{\text{in}}, \quad (3)$$

which imposes a right-going wave with amplitude A and which absorbs the left-going planar waves; $\partial u / \partial n$ denotes the derivative of the function u in the direction defined by the outward directed unit normal n on Γ_{in} . Moreover, the boundary condition

$$\frac{\partial u}{\partial n} = 0 \quad (4)$$

is imposed on the sound-hard walls of the device, on the symmetry boundary Γ_{sym} , and also on Γ_{out} , since the effect of the condition on the PML's terminating boundary is not significant [29]. The presence of the PML changes the state equation (2) to

$$\nabla \cdot (\mathbf{D}\nabla u) + k^2 \gamma u = 0 \quad \text{in } \Omega, \quad (5)$$

where $\mathbf{D} = \text{diag}(\gamma_2/\gamma_1, \gamma_1/\gamma_2)$ and $\gamma = \gamma_1\gamma_2$ with γ_1 and γ_2 complex-valued functions different from unity only within the PML [35, 18].

The variational form of problem (5) with boundary conditions (3) and (4) reads

find $u \in H^1(\Omega)$ such that

$$\int_{\Omega} \nabla q \cdot (\mathbf{D}\nabla u) - k^2 \int_{\Omega} \gamma q u + ik \int_{\Gamma_{\text{in}}} q u = 2ikA \int_{\Gamma_{\text{in}}} q, \quad \forall q \in H^1(\Omega), \quad (6)$$

where $H^1(\Omega) = \{q \in L^2(\Omega) \mid \partial q / \partial x_j \in L^2(\Omega), j \in \{1, 2\}\}$. Bramble & Pasciak [6] show existence, uniqueness, and exponential convergence to the infinite exterior Helmholtz problem for a finite PML approximation of an acoustics problem very similar to variational problem (6). The shape of the boundary Γ_d in figure 2 is subject to design. In the standard implementation of boundary shape optimization, the computational domain is modified, and it is remeshed, or the mesh is deformed, at each design cycle. We propose a different approach that does not require remeshing or mesh deformations. We assume that Γ_d constitutes a part of the boundary of a domain Ω_d that contains a sound-hard material, as in figure 2, and we extend the computational domain Ω to $\hat{\Omega}$, which also includes Ω_d , so that $\hat{\Omega} = \bar{\Omega} \cup \bar{\Omega}_d$. By introducing the function $\alpha : \hat{\Omega} \rightarrow \{\varepsilon, 1\}$, such that $\alpha(\mathbf{x}) = \varepsilon$ when $\mathbf{x} \in \Omega_d$ and $\alpha(\mathbf{x}) = 1$ when $\mathbf{x} \in \Omega$, with $0 \leq \varepsilon \ll 1$, we can formulate the following extended problem:

find $p \in H^1(\hat{\Omega})$ such that

$$\int_{\hat{\Omega}} \alpha \nabla q \cdot (\mathbf{D}\nabla p) - k^2 \int_{\hat{\Omega}} \alpha \gamma q p + ik \int_{\Gamma_{\text{in}}} q p = 2ikA \int_{\Gamma_{\text{in}}} q, \quad \forall q \in H^1(\hat{\Omega}). \quad (7)$$

By choosing $\varepsilon = 0$ in problem (7), we recover problem (6). However, by choosing the lower bound ε different from zero, we will obtain a uniquely solvable problem, with no ambiguity in the definition of p within Ω_d . This strategy is standard when using the material distribution approach to topology optimization [4, § 1.2.1]. For strongly elliptic state equations (in our case that would be for very small values of k), it is known that $p_\varepsilon|_\Omega \rightarrow p$, where p_ε is the ε -perturbed problem on $\hat{\Omega}$ and p the original solution on Ω , with a convergence rate of ε in $H^1(\Omega)$ [37]. We do not know of any error analysis for the general Helmholtz equation, but in § 6, we numerically check in a “typical” case that the errors are reasonably small.

A major difference between topology optimization and our approach is that in topology optimization, an optimal distribution of material in a given domain is sought, meaning that the function α is the design variable. Since we aim for boundary shape optimization, the function α only serves as an intermediate step that enables the utilization of the equation’s coefficients to represent the geometry of the horn.

We are interested in finding the horn shape that minimizes the reflections measured on Γ_{in} . Thus we introduce the function J_k defined as the absolute ratio between the amplitude of a left and a right-going wave,

$$J_k(\alpha) = \frac{|\langle p \rangle_{\text{in}} - A|}{|A|}, \quad (8)$$

where k denotes the wave number we optimize for and $\langle p \rangle_{\text{in}}$ denotes the average value of p measured on Γ_{in} , that is

$$\langle p \rangle_{\text{in}} = \frac{1}{|\Gamma_{\text{in}}|} \int_{\Gamma_{\text{in}}} p. \quad (9)$$

Given a generic parameterization of the design boundary $\Gamma_d \subset \partial\Omega_d$ with control variable ϑ , and a set Θ of admissible designs, the optimization problem is formulated as

$$\min_{\vartheta \in \Theta} \mathcal{J}(\alpha(\vartheta)) = \frac{1}{2} \sum_{k \in \mathbf{K}} J_k^2(\alpha(\vartheta)) + \frac{\mu}{2} \|\vartheta\|^2, \quad (10)$$

where \mathbf{K} denotes the set of the wave numbers subject to optimization and the term $\mu \|\vartheta\|^2 / 2$ with $\mu \geq 0$ introduces a so-called Tikhonov regularization, which for $\mu > 0$ can be used to balance the need for small J_k and small values of the design variables.

3 Discretization

The state equation (7) is discretized using the Finite Element Method (FEM). For that purpose we use a structured grid consisting of M square elements E_j of side length h .

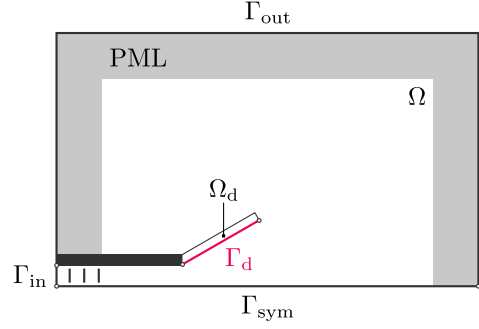


Fig. 2 The truncated computational domain.

Furthermore, we introduce \mathbf{D}_h , γ_h , and α_h , the element-wise constant representations of \mathbf{D} , γ , and α , respectively. The discretized variational form of problem (7) reads

find $p_h \in V_h \subset H^1(\hat{\Omega})$ such that

$$\int_{\hat{\Omega}} \alpha_h \nabla q_h \cdot (\mathbf{D}_h \nabla p_h) - k^2 \int_{\hat{\Omega}} \alpha_h \gamma_h q_h p_h + ik \int_{\Gamma_{\text{in}}} q_h p_h = 2ikA \int_{\Gamma_{\text{in}}} q_h, \quad \forall q_h \in V_h, \quad (11)$$

where the space V_h consists of continuous, element-wise bi-quadratic functions. The FE solution p_h can be written as

$$p_h = \sum_{j=1}^N p_j \varphi_j, \quad (12)$$

where N is the number of degrees of freedom, p_j are the nodal values, and φ_j are the basis functions of V_h , that is $V_h = \text{span}\{\varphi_j\}$, $j = 1, \dots, N$. The variational problem (11) can be written, using matrix notation, in the form

$$(\mathbf{K}(\alpha_h) - k^2 \mathbf{M}(\alpha_h) + ik \mathbf{B}) \mathbf{p} = 2ikA \mathbf{B} \mathbf{e}, \quad (13)$$

where $\mathbf{p} = (p_1, \dots, p_N)^T$ and $\mathbf{e} = (1, \dots, 1)^T$ are vectors of length N , and

$$K_{ij} = \int_{\hat{\Omega}} \alpha_h \nabla \varphi_i \cdot (\mathbf{D}_h \nabla \varphi_j), \quad M_{ij} = \int_{\hat{\Omega}} \alpha_h \gamma_h \varphi_i \varphi_j, \quad (14)$$

$$B_{ij} = \int_{\Gamma_{\text{in}}} \varphi_i \varphi_j,$$

are the components of the corresponding $N \times N$ matrices.

4 Design boundary parameterization

The choice of parameterization is significant in design optimization since the parameterization limits the feasible shapes. In general, this means that different parameterizations lead to different optimal shapes. Here, we suggest a parameterization based on a discrete curvature.

Let Γ_d be the design boundary illustrated in figures 2 and 3. We assume that the horn flare Γ_d is a polygon that

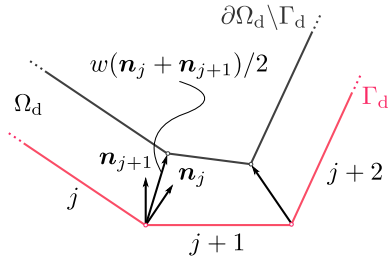


Fig. 3 The back side of the horn is generated by linear interpolation of the points $w(\mathbf{n}_j + \mathbf{n}_{j+1})/2$, where w is a constant and \mathbf{n}_j and \mathbf{n}_{j+1} are the normals to the segments j and $j+1$, respectively.

comprises S line segments, all of length ℓ . We assign the angle differences ϑ_j between the segments j and $j-1$, $j=1, \dots, S$, as our design variables; the zeroth segment corresponds to the waveguide. The quantity ϑ_j/ℓ corresponds to a local discrete curvature of Γ_d .

Computational experience suggests that the reflections at Γ_{in} are not sensitive to the shape of the back side $\partial\Omega_d \setminus \Gamma_d$ of the horn. Thus, the benefit from an independent control of the back side of the horn is negligible. For that reason, $\partial\Omega_d \setminus \Gamma_d$ is formed by linear interpolation of the points $w(\mathbf{n}_j + \mathbf{n}_{j+1})/2$, where \mathbf{n}_j and \mathbf{n}_{j+1} are the normals to the segments j and $j+1$, respectively, and w is a parameter guiding the material thickness. Note that, as shown in figure 3, this construction causes the actual thickness of the horn to vary slightly depending on the value of the control variables ϑ_j .

In our numerical experiments, we define $\partial\Omega_d$ such that $\partial\Omega_d \cap \overline{E_n}$ is a straight line segment for all elements such that $\Omega_d \cap \overline{E_n} \neq \emptyset$. This will constitute an approximation of the earlier description of $\partial\Omega_d$ as a sequence of segments of length ℓ for the case when different segments meet at an angle inside the element. However, since in all numerical experiments, the segment length ℓ is much longer than element size h , the effects of this approximation will be minor; only the elements in which two segments meet inside the element will be (slightly) affected.

Having constructed the design domain Ω_d , we define the element-wise constant material function α_h over $\hat{\Omega}$ by

$$\alpha_n = \alpha_h|_{E_n} = 1 + (\varepsilon - 1) \frac{|E_n \cap \Omega_d|}{|E_n|}, \quad n \in \{1, 2, \dots, M\}, \quad (15)$$

where E_n denotes the n th element of the computational mesh and $|\cdot|$ denotes the area occupied by the corresponding set. To compute the constant values α_n according to expression (15), we first traverse the boundary $\partial\Omega_d$ and compute the areas $|E_n \cap \Omega_d|$, as briefly described below, for each element intersected by the boundary. For elements E_n not being intersected by the boundary $\partial\Omega_d$, $E_n \cap \Omega_d$ is either E_n or \emptyset .

Let E_r be the reference element $[0, 1] \times [0, 1]$ and assume that $\partial\Omega_d$ is positively oriented. For each element

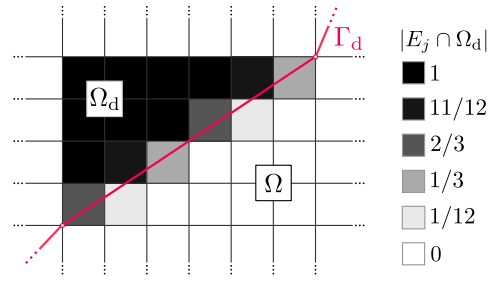


Fig. 4 The values of the area $|E_n \cap \Omega_d|$ used to find the values α_n of the characteristic function α_h for a segment of the design boundary Γ_d with slope $2/3$ on a grid that consists of elements of side length $h=1$.

E_n intersected by the boundary, we define an affine map $\mathcal{T}_n : E_n \rightarrow E_r$ consisting of a scaling, a rotation, and a translation. There are several possible choices of \mathcal{T}_n ; here, we choose \mathcal{T}_n such that $\mathcal{T}_n \partial\Omega_d$ is positively oriented and enters E_r from the left side. Once, we have \mathcal{T}_n , we invoke a routine that calculates $|E_r \cap \mathcal{T}_n(\Omega_d)|$. When we traverse the boundary, in addition to computing the relative areas $|E_n \cap \Omega_d|/|E_n|$, we also record the points at which the boundary enters and exits the element E_n . The above boundary sweep takes case of all elements E_n such that $\overline{E_n} \cap \partial\Omega_d \neq \emptyset$. For all other elements, we have that either $E_n \subset \Omega$ or $E_n \subset \Omega_d$ and thus by expression (15) α_n is either 1 or ε .

The computational complexity of the boundary sweep described above is linear in the number of elements intersecting the boundary. Thus, the overall complexity of computing or updating the pixel values α_n is at most linear in number of elements in Ω_d . In our implementation, the time spend to compute and update these pixel values is negligible in comparison to the time required to assemble and solve the linear system (13).

5 Sensitivity analysis

Our optimization problem, the discrete version of problem (10), is a non-linear least-squares problem, which we solve using a gradient-based method with a Gauss–Newton Hessian approximation [26, Ch. 10]. Such a Hessian approximation requires gradients of each component of the objective function. The objective function in problem (10) comprises a Tichonov regularization term plus a sum of functions J_k^2 , where k represents a wave number we optimize for and J_k measures, as defined in expression (8), the relative amplitude of the reflected wave. The square amplitude of the reflected wave can be written

$$J_k^2(\alpha_h) = \frac{|\langle p_h \rangle_{\text{in}} - A|^2}{|A|^2} = \frac{1}{|A|^2} \left(f_{1,k}^2(\alpha_h) + f_{2,k}^2(\alpha_h) \right), \quad (16)$$

where

$$f_{1,k}(\alpha_h) = \Re(\langle p_h \rangle_{\text{in}} - A) \quad (17)$$

and

$$f_{2,k}(\alpha_h) = \Im(\langle p_h \rangle_{\text{in}} - A), \quad (18)$$

respectively. Here, p_h is the solution of discrete state problem (11) with the current design α_h and wave number k . That is, our objective function can be written as the sum of squares of functions of the type $f_{1,k}$ and $f_{2,k}$ above plus the Tichonov term. The gradient of the Tichonov term with respect to the design variables is immediate. The real and imaginary part of the complex amplitude $\langle p_h \rangle_{\text{in}} - A$ of the reflected wave depend on the design variable ϑ_j through the function α_h . Let $f_{i,k}(\theta_j) = f_{i,k}(\alpha_h(\theta_j))$. By the chain rule, we have that

$$\frac{\partial f_{i,k}}{\partial \vartheta_j} = \sum_{n=1}^M \frac{\partial f_{i,k}}{\partial \alpha_n} \frac{\partial \alpha_n}{\partial \vartheta_j} \quad \text{for } i = 1, 2. \quad (19)$$

5.1 Variations with respect to material changes

Let α_h be a given, element-constant, positive function in problem (11) representing the current design, and let $\delta\alpha_h$ be an arbitrary variation of α_h . The first variation of $f_{1,k}$ and $f_{2,k}$ are given by

$$\begin{aligned} \delta f_{1,k}(\alpha_h) &= \delta \Re(\langle p_h \rangle_{\text{in}} - A) = \Re(\langle \delta p_h \rangle_{\text{in}}), \\ \delta f_{2,k}(\alpha_h) &= \delta \Im(\langle p_h \rangle_{\text{in}} - A) = \Im(\langle \delta p_h \rangle_{\text{in}}), \end{aligned} \quad (20)$$

where δp_h is the first variation of p_h corresponding to $\delta\alpha_h$. To compute $\langle \delta p_h \rangle_{\text{in}}$, we take the variations of the discrete state equation (11) with respect to $\delta\alpha_h$ and get that

$$\begin{aligned} \int_{\hat{\Omega}} \delta\alpha_h \nabla q_h \cdot (\mathbf{D} \nabla p_h) + \int_{\hat{\Omega}} \alpha_h \nabla q_h \cdot (\mathbf{D} \nabla \delta p_h) \\ - k^2 \int_{\hat{\Omega}} \delta\alpha_h \gamma q_h p_h - k^2 \int_{\hat{\Omega}} \alpha_h \gamma q_h \delta p_h \\ + ik \int_{\Gamma_{\text{in}}} q_h \delta p_h = 0 \end{aligned} \quad (21)$$

holds for all $q_h \in V_h$. In particular, the above expression holds for $q_h = p_h$. Taking into consideration that the matrix \mathbf{D} is diagonal, setting $q_h = p_h$, and rearranging the terms yields that

$$\begin{aligned} \int_{\hat{\Omega}} \alpha_h \nabla p_h \cdot (\mathbf{D} \nabla \delta p_h) - k^2 \int_{\hat{\Omega}} \alpha_h \gamma p_h \delta p_h + ik \int_{\Gamma_{\text{in}}} p_h \delta p_h \\ = k^2 \int_{\hat{\Omega}} \delta\alpha_h \gamma p_h^2 - \int_{\hat{\Omega}} \delta\alpha_h \nabla p_h \cdot (\mathbf{D} \nabla p_h). \end{aligned} \quad (22)$$

The left side of the above expression is the same as the left side of the discrete state equation (11) with the particular choice $q_h = \delta p_h$. Moreover, by construction all admissible design changes $\delta\alpha_h \equiv 0$ within the PML (No part of the design boundary will be located in the PML.). Hence, we conclude that

$$2ikA \int_{\Gamma_{\text{in}}} \delta p_h = k^2 \int_{\hat{\Omega}} \delta\alpha_h p_h^2 - \int_{\hat{\Omega}} \delta\alpha_h \nabla p_h \cdot \nabla p_h. \quad (23)$$

Using the definition of $\langle \cdot \rangle_{\text{in}}$ in expression (9), we may from expressions (20) and (23) identify the partial derivatives of $f_{1,k}$ and $f_{2,k}$ with respect to changes in α_n (defined in expression (15)) as

$$\frac{\partial f_{1,k}}{\partial \alpha_n} = \Re \left(\frac{1}{2ikA|\Gamma_{\text{in}}|} \int_{E_n} (k^2 p_h^2 - \nabla p_h \cdot \nabla p_h) \right), \quad (24)$$

and

$$\frac{\partial f_{2,k}}{\partial \alpha_n} = \Im \left(\frac{1}{2ikA|\Gamma_{\text{in}}|} \int_{E_n} (k^2 p_h^2 - \nabla p_h \cdot \nabla p_h) \right), \quad (25)$$

respectively.

5.2 Variations with respect to angle changes

To calculate the derivative (19) of the objective function with respect to design variables ϑ_j , we also need the Jacobian matrix $\partial\alpha_n/\partial\vartheta_j$. Recall from § 4 that the design variables $\vartheta_1, \dots, \vartheta_S$ are the angles between successive segments in the inside of the horn, and that the horn outside is passively displaced. Thus, when applying an angle variation $\delta\vartheta_1$ of the first design variable and keeping all other design variables constant, *all* segments, on the inside as well as on the outside of the horn, will be displaced. Moreover, all segments (with two exceptions detailed below) will be subject to a solid body rotation around an axis at the start of the first segment. The exceptions are the two last segments (on the horn back side). Since the last segment is fixed at its end point at the waveguide, the two last segments will be displaced in a more complicated motion than the solid body rotation that all other segments will experience. When applying an angle variation $\delta\vartheta_2$, the first segment will not move, but all other segments, (except, again, the last two) will experience a solid body rotation around an axis located at the start of the second segment. This patterns continues for all the design variables.

Now consider an arbitrary design-variable variation $\delta\vartheta_j$, and let E_n be an element with a nonvanishing intersection with any of the segments affected by $\delta\vartheta_j$, according to the above discussion. We exclude the case when E_n intersects any of the last two segments and discuss this case separately below.

Recall from section 4 that the value α_n of the function α_h in element E_n is computed by using an affine mapping taking E_n to the reference element E_r such that $\mathcal{T}_n \partial\Omega_d$ is positively oriented and enters the left side of E_r . Hence, it is sufficient to consider only this case. We consider the geometry under the affine map \mathcal{T}_n , which yields a situation as illustrated in figure 5. Let x_c be the point at the beginning of the mapped segment j , that is, the axis of rotation when changing ϑ_j . Moreover, let x_{in} and x_{out} denote the points where $\mathcal{T}_n \partial\Omega_d$ enters and exits element E_r , respectively. We also define the line $\ell_c = \{x \mid x = x_c + t\mathbf{n}, t \in \mathbb{R}\}$, where \mathbf{n} is the

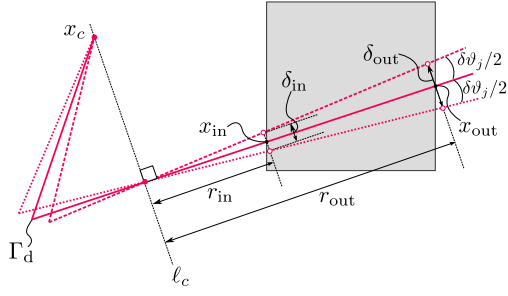


Fig. 5 Changing the design variable ϑ_j results in a solid body rotation. We compute the first variation of the area fraction $|E_n \cap \Omega_d|/|E_n|$ by mapping the complete design using the affine mapping \mathcal{T}_n , taking E_n to the unit size reference element E_r .

normal to the boundary $\mathcal{T}_n \partial \Omega_d$ in E_r . The normal offset distances δ_{in} and δ_{out} are to first order given by $r_{\text{in}} \delta \vartheta_j$ and $r_{\text{out}} \delta \vartheta_j$, where r_{in} and r_{out} , illustrated in figure 5, are the distances from the line ℓ_c to x_{in} and x_{out} , respectively. Moreover, the change of $|E_r \cap \mathcal{T}_n \Omega_d|$ is to first order equal to the negative area of the trapezoid with corners marked with circles in figure 5, that is

$$\begin{aligned} \delta |E_r \cap \mathcal{T}_n \Omega_d| &= -\frac{1}{2} (\delta_{\text{in}} + \delta_{\text{out}}) (r_{\text{out}} - r_{\text{in}}) \\ &= -\frac{1}{2} (r_{\text{out}}^2 - r_{\text{in}}^2) \delta \vartheta_j. \end{aligned} \quad (26)$$

Combining expressions (15) and (26) and using that area quotients are invariant under affine mappings yields

$$\frac{\partial \alpha_n}{\partial \vartheta_j} = \frac{1 - \varepsilon}{2h^2} (r_{\text{out}}^2 - r_{\text{in}}^2). \quad (27)$$

As noted above, the assumption of a solid body rotation around the initial point of segment j that underlies the reasoning above does not hold for elements E_n that intersects the two last segments (at the backside of the horn). A finite-difference approximation is therefore used for these elements instead of formula (27).

In the particular case when a segment coincides with an element boundary, the derivative $\partial \alpha_n / \partial \vartheta_j$ is not well defined in that the left and the right derivatives differs for the elements bordering this segment. However, in this case, the right derivative will coincide with the left derivative for the neighboring element. Since it can be expected that the different $\partial f_{i,k} / \partial \alpha_n$ associated with neighboring cells will be very close, it follows from expression (19) that the left and right derivatives of the objective function with respect to the design variable ϑ_j will be the same up to the difference in $\partial f_{i,k} / \partial \alpha_n$ between neighboring cell. Thus, the discontinuities of $\partial \alpha_n / \partial \vartheta_j$ will only have a minor effect on the total derivative (19) as long as we consistently choose either the right or left derivative when computing $\partial \alpha_n / \partial \vartheta_j$ (we choose the right).

Another way of handling this non-differentiability issue is to use a filtering procedure that resulting in a smooth

transaction between the left and right derivative. Yet another alternative is to replace the volume fraction in expression (15) by a filtered version in which α_n is defined through the convolution of the characteristic function with a continuous piecewise smooth and compact kernel. For a more detailed discussion on such strategies, we refer to Norato et al. [27].

6 Numerical experiments

6.1 General setup

In the numerical experiments, we set the complex amplitude of the right-going wave in equation (7) to $A = 1$ and the sound speed to $c = 345$ m/s. The computational mesh consists of $M = n_x \cdot n_y$ square bi-quadratic elements of side length $h = 0.1 \cdot 2^{-5}$ m, where $n_x = 1/h$ and $n_y = 0.6/h$. Additional dimensional characteristics include the width of the material that forms the waveguide $w = 0.025$ m, the width of the truncated waveguide boundary $|\Gamma_{\text{in}}| = 0.05$ m, and the width of the PML $\delta = 0.1$ m. Moreover, the length ℓ of each of the S segments that constitute the design boundary Γ_d are chosen so that $|\Gamma_d| = S\ell = 0.4$ m.

Optimization problem (10) is supplemented with the constraints $|\vartheta_j| \leq C\ell$, where the constant $C = 20$ rad/m. This constant is chosen to admit the formation of back-folded and even spiral horns; if the horn curves as much as possible, the maximum angle change is $SC\ell = 8$ rad. Due to the nature of the parameterization, the enforced constraints provide bounds on the local curvature and consequently affects the smoothness of the feasible designs.

The purpose of the following experiment is to investigate the effect of the lower bound ε on the accuracy of the solution p_h . In other words, we study the effect of representing the horn through varying coefficients of the state equation. We select the fixed horn shape with corresponding raster representation shown in figure 6. The shape is constructed by selecting the constant design variables $\vartheta_j = 2\ell$ for each $j = 1, \dots, S$. This polygonal shape approaches, as $S \rightarrow \infty$, a segment with length 0.4 m of a circle with radius $R = 1/2$. (Recall that $\vartheta_j / \ell = 2 = 1/R$ represents a discrete curvature).

For this horn shape, we generate the reflection spectra using the varying coefficient approach discussed in sections 3 and 4 as well as by discretizing equation (6) with the finite-element method using an unstructured body-fitted mesh. The first illustration in figure 7 presents the results from three numerically generated reflection spectra for the geometry shown in figure 6. The thick light-colored line represents the reference spectrum J_k^{ref} obtained using the body-fitted approach, implemented in FreeFem++ (www.freefem.org/ff++/), using an unstructured mesh employing triangular, second-order Lagrange elements (P^2)

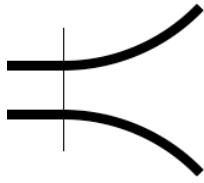


Fig. 6 The horn for which reference spectra are generated and compared.

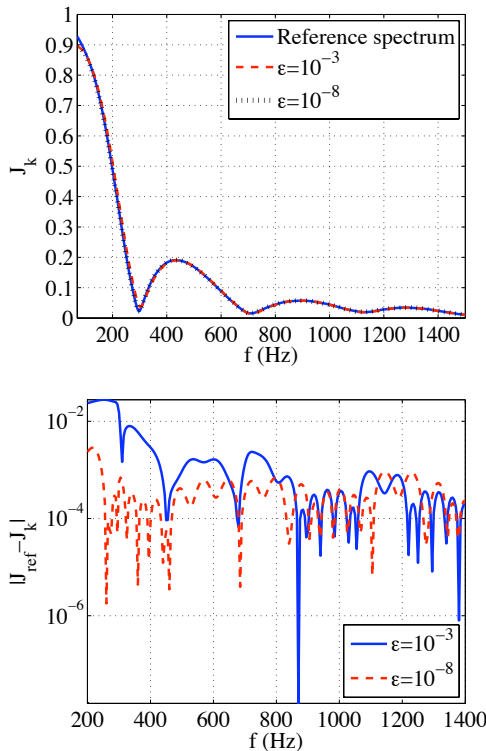


Fig. 7 Top: reflection spectra generated by using body-fitted and variable-coefficient representation of the horn in figure 6. Bottom: absolute value of difference between the spectra generated by using the body-fitted and variable-coefficient representation.

and a piecewise linear boundary representation. In this experiment, we numerically solve (6) on a semi-disk with radius 2 m employing the lowest-order Engquist–Majda radiation boundary condition [11] on the outer boundary. The two other spectra have been generated using the varying coefficient method with $\varepsilon = 10^{-3}$ and 10^{-8} . Visually, the three spectra in the first illustration in figure 7 are indistinguishable. The second illustration in this figure shows the difference $|J_k^{\text{ref}} - J_k|$, where J_k refers to the spectra generated with the varying coefficient method, as a function of frequency. The difference tends to be larger at low frequencies, but for $\varepsilon = 10^{-8}$, this difference is almost uniformly small in the studied frequency range. For the remainder of our numerical experiments, we set $\varepsilon = 10^{-8}$.

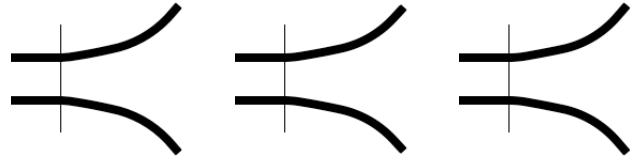


Fig. 8 Optimized horns for 600 Hz using (from left to right) $S = 16$, $S = 32$, and $S = 64$ segments.

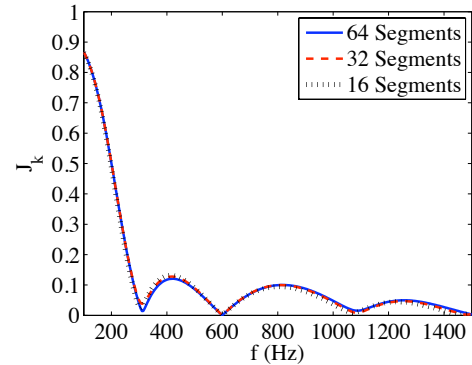


Fig. 9 Reflection spectra for the horns in figure 8.

6.2 Studies with respect to the number of segments

We numerically solve the non-linear least-squares problem (10) using the Matlab function `lsqnonlin`, with the large scale option and default termination conditions. The algorithm employs an interior trust-region method for globalization and to account for the bound constraints on the design variables [9]. As we will see, the values of all terms in the objective function are small at optimum, hence the Gauss–Newton method is expected to show a rapid local convergence (quite similar to that of Newton’s method [26, § 10.2]). For all experiments we use a so-called continuation approach, known to prevent trapping at a local minimum in certain cases [32]. That is, we solve a sequence of optimization problems starting by the problem with $\mu = 1$. The solution of that problem is then used as an initial guess to the next problem, which is solved with regularization parameter $\mu/10$. We continue decreasing μ with a factor $1/10$ until we solve the weakly regularized problem for $\mu = 10^{-8}$.

In the following experiments, we study how the optimal shapes depend on the number S of segments that constitute the design boundary Γ_d . We minimize the reflections for both single and multi-frequency objectives; for each objective, we generate optimal designs with $S = 16$, $S = 32$, and $S = 64$ segments representing Γ_d , respectively.

Figures 8 and 10 show horns optimized for 600 Hz and 1000 Hz, respectively. We note that in those cases the raster representations are almost identical; it is even hard to visually decide upon the number S of segments used to represent the design boundary Γ_d .

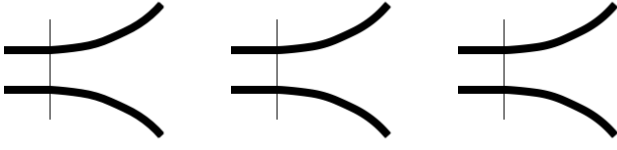


Fig. 10 Optimized horns for 1000 Hz using (from left to right) $S = 16$, $S = 32$, and $S = 64$ segments.

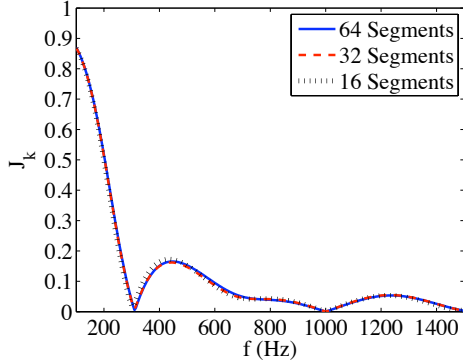


Fig. 11 Reflection spectra for the horns in figure 10.

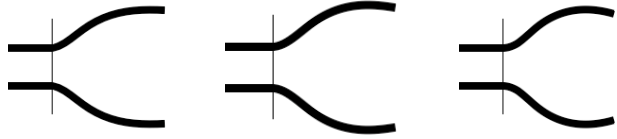


Fig. 12 Optimized horns for 200 Hz using (from left to right) $S = 16$, $S = 32$, and $S = 64$ segments.

In figure 12, we present devices optimized for 200 Hz, whereas the corresponding spectra are shown in figure 13. We note that the length of the device here is less than one quarter of the wavelength ($|\Gamma_d| = 0.4$ m and $\lambda = 1.725$ m). As indicated by figure 7, this length is in general too short for a horn to function as an efficient transmitter. The optimized devices start acquiring a resonator-like shape, and their transmission properties are generally quite bad, except at the design frequency. For this more difficult optimization problem, we also see a certain dependency on the number of line segments. Nevertheless, the shapes of the optimized horns do not show extreme differentiations with respect to the number of line segments S , and the horns appear to be regular in the sense that the design parameters ϑ_j do not change rapidly from segment to segment. The latter is mainly due to the parameterization and the imposed curvature constraints in the formulation of the minimization problem, which do not allow large variations. An additional smoothing effect comes from the raster representation of the horn that introduces a one pixel ambiguity regarding the exact boundary shape [31, 7].

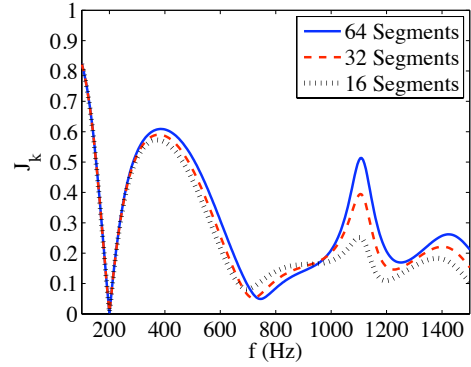


Fig. 13 Reflection spectra for the horns in figure 12.

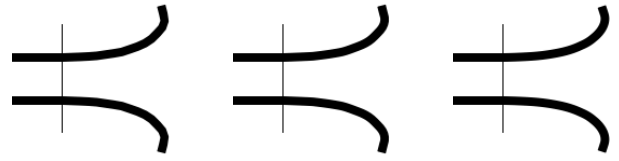


Fig. 14 Optimized horns for 466–1480 Hz using (from left to right) $S = 16$, $S = 32$, and $S = 64$ segments.

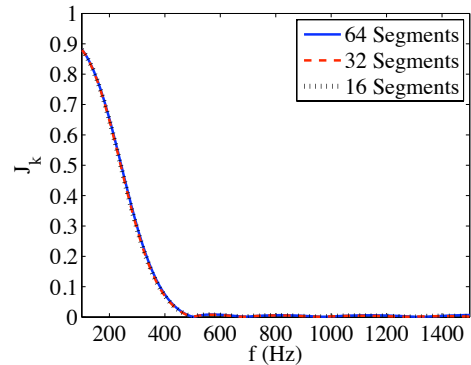


Fig. 15 Reflection spectra for the horns in figure 14.

Figures 14 and 15 show optimal horns and corresponding spectra when optimizing over a relatively wide frequency band, 466–1480 Hz. More precisely, the horns are optimized for minimal reflections at the frequencies $f_n = 440 \cdot 2^{n/12}$ for $n = 1, 2, \dots, 21$. The reflection spectra in figure 15 are practically identical. The folding at the end of the horn and the almost straight part immediately after the vertical line (that indicates the starting point of the design boundary Γ_d) suggest that the full length $|\Gamma_d| = 0.4$ m is not needed to achieve a design that performs as desired.

The resulting horns and the corresponding spectra from our final experiment are presented in figures 16 and 17. Here, we optimize for the frequency range 293–392 Hz, that is, we minimize the reflections at the frequencies $f_n = 220 \cdot 2^{n/12}$ for $n = 5, 6, \dots, 10$. We observe that the spectra are almost independent of the number of segments used, especially close to the optimization frequency band. It is worth

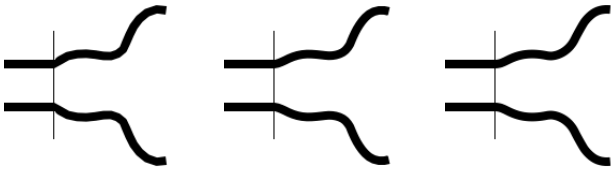


Fig. 16 Optimized horns for 293–392 Hz using (from left to right) $S = 16$, $S = 32$, and $S = 64$ segments.

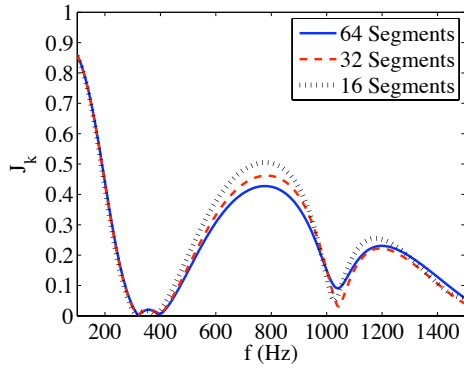


Fig. 17 Reflection spectra for the horns in figure 16.

mentioning that the resulting designs are far from what is considered a typical horn shape, similarly as discussed in the single-frequency optimization for 200 Hz.

For all experiments, the optimization was able to generate designs that almost perfectly transmit at the target frequencies independent of the number of line segments S representing Γ_d . By increasing S , the obtained raster representations appears to converge to particular designs in all studied cases. An overall conclusion is that the parameterization is well-behaved, meaning that the formation of oscillatory boundaries is avoided.

7 Discussion

The standard implementation of boundary shape optimization involves deformations of the computational mesh so that it conforms to the modified boundary. **In contrast, the geometry representation used here does not need mesh deformations or remeshing, which allows the use of a parameterization that is able to curve the design boundary in ways that would be more difficult to admit in an implementation that relies on mesh deformations.** The chosen parameterization has the advantage of inherently promoting smooth design updates. The optimal horns generated here perform remarkably well even for waves of wavelengths that are long compared to the size of the horn.

The horns generated for the same objective but with different number of line segments have surprisingly similar raster representations. In figure 18, we plot the angle formed by each segment and the horizontal axis as a func-

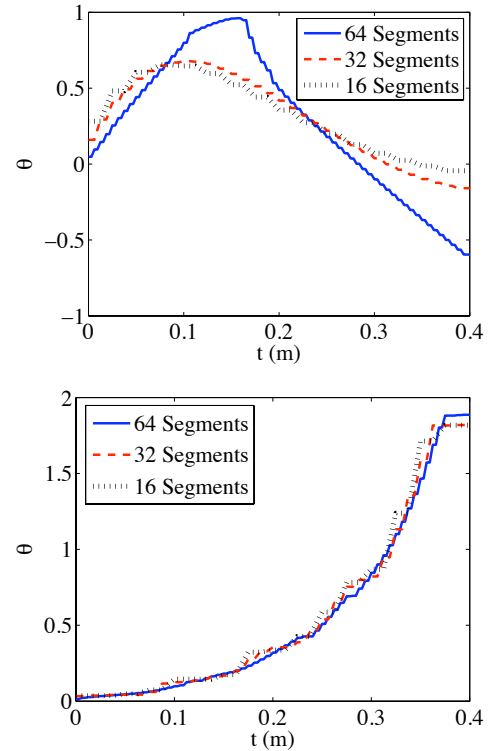


Fig. 18 Angle with respect to the horizontal axis as a function of arc length for different number S of segments comprising the design boundary. The top illustration refers to the horns optimized for 200 Hz, whereas the lower to the horns optimized for the frequency band 466–1480 Hz.

tion of the arc length of the design boundary for two of our experimental setups. The top diagram refers to the design optimized for 200 Hz, whereas the bottom one corresponds to the horns optimized for the frequency band 466–1480 Hz. The three different line styles in each plot refer to the number S of line segments comprising the design boundary Γ_d . For the 200 Hz case, we conclude that the design obtained using $S = 16$ and $S = 32$ are relatively close to each other, while there is a more intense change regarding the $S = 64$ case. By comparing the horn flares in figure 12, all three flare shapes suggest a concave design, in particular, these features are more pronounced in the 64-segment horn. The diagram for the frequency band 466–1480 Hz illustrates that the three optimal designs in figure 14 are nearly identical. The rest of the experiments performed in our study are similar to the latter case.

Future work includes studies where a hybrid shape–topology optimization approach is adopted, meaning that the boundary shape optimization is combined with topology optimization [35]. According to our experience, such an approach may resolve the problem of designing an efficient transmitter for low frequencies. A hybrid shape–topology optimization approach would also be beneficial in order to design, over a substantial frequency band, a true con-

stant directivity horn that also shows ideal transmission properties.

There are various ways in which the current parameterization could be generalized to more general surfaces in three space dimensions. One way is to start with a curve γ_d , parameterized as in § 4, and generate the design surface by extruding straight lines perpendicular to each segment. The twist angles of the extruded lines, or perhaps rather the angle change from one segment to the next, would constitute a second set of design variables, in addition to those generating the curve γ_d . This approach would generate (as the segment length $\ell \rightarrow 0$) intrinsically flat *developable surfaces*, a type of surface that can be unrolled onto a flat plate. Such surfaces can be constructed from flat sheets of material without stretching, and are often used in the design of, for instance, ship hulls and aircraft fuselages and wings [33, § 8.17]. Another possibility would be general *ruled surfaces* [33, § 8.17]. (Developable surfaces are special cases of ruled surfaces). Ruled surfaces are generated by linear interpolation between two design curves γ_{d1} and γ_{d2} . A third possibility would be *Coons surfaces*, that is, bilinear interpolation between four connected boundary curves $\gamma_{d1}, \dots, \gamma_{d4}$, or higher-degree generalizations of Coons surfaces [30, § 3.7]. Extensions of the curvature-based parameterization to completely general smooth surfaces would, however, be challenging. Such a generalization would involve parameterization of the two principal curvatures as well as the orientation of the principal directions. Whether such an approach would be feasible or practical is an open question.

References

- Allaire, G., Jouve, F., Toader, A.M.: A level-set method for shape optimization. *C. R. Acad. Sci. Paris Sér. I Math.* **334**(12), 1125–1130 (2002). DOI 10.1016/S1631-073X(02)02412-3
- Allaire, G., Jouve, F., Toader, A.M.: Structural optimization using sensitivity analysis and a level-set method. *J. Comput. Phys.* **194**(1), 363–393 (2004). DOI 10.1016/j.jcp.2003.09.032
- Bängtsson, E., Noreland, D., Berggren, M.: Shape optimization of an acoustic horn. *Comput. Methods Appl. Mech. Engrg.* **192**, 1533–1571 (2003). DOI 10.1016/S0045-7825(02)00656-4
- Bendsøe, M.P., Sigmund, O.: *Topology Optimization. Theory, Methods, and Applications.* Springer (2003)
- Bobaru, F., Rachakonda, S.: $E(FG)^2$: a new fixed-grid shape optimization method based on the element-free Galerkin mesh-free analysis. *Struct. Multidiscip. Optim.* **32**, 215–228 (2006). DOI 10.1007/s00158-006-0018-x
- Bramble, J.H., Pasciak, J.E.: Analysis of a finite PML approximation for the three dimensional time-harmonic Maxwell and acoustic scattering problems. *Math. Comp.* **76**(258), 597–614 (2007). DOI 10.1090/S0025-5718-06-01930-2
- Bruns, T.E., Tortorelli, D.A.: Topology optimization of non-linear elastic structures and compliant mechanisms. *Computer Methods in Applied Mechanics and Engineering* **190**, 3443–3459 (2001). DOI 10.1016/S0045-7825(00)00278-4
- Burger, M., Hackl, B., Ring, W.: Incorporating topological derivatives into level set methods. *J. Comput. Phys.* **194**(1), 344–362 (2004). DOI 10.1016/j.jcp.2003.09.033
- Coleman, T.F., Li, Y.: An interior trust region approach for nonlinear minimization subject to bounds. *SIAM Journal on Optimization* **6**, 418–445 (1996)
- Duysinx, P., Miegroet, L., Jacobs, T., Fleury, C.: Generalized shape optimization using X-FEM and level set methods. In: M.P. Bendsøe, N. Olhoff, O. Sigmund (eds.) *IUTAM Symposium on Topological Design Optimization of Structures, Machines and Materials, Solid Mechanics and Its Applications*, vol. 137, pp. 23–32. Springer Netherlands (2006)
- Engquist, B., Majda, A.: Absorbing boundary conditions for numerical simulation of waves. *Math. Comp.* **31**(139), 629–651 (1977)
- Frei, W., Johnson, H., Choquette, K.: Optimization of a single defect photonic crystal laser cavity. *J. Appl. Phys.* **103**, 033,102–1–033,102–7 (2008). DOI 10.1063/1.2838173
- Frei, W.R., Johnson, H.T., Tortorelli, D.A.: Optimization of photonic nanostructures. *Comput. Methods Appl. Mech. Engrg.* **197**(41–42), 3410–3416 (2008). DOI 10.1016/j.cma.2008.03.030
- Frei, W.R., Tortorelli, D.A., Johnson, H.T.: Geometry projection method for optimizing photonic nanostructures. *Opt. Lett.* **32**(1), 77–79 (2007). DOI 10.1364/OL.32.000077
- Gunzburger, M.D.: *Perspectives in Flow Control and Optimization.* SIAM, Philadelphia (2003)
- Haftka, R.T., Grandhi, R.V.: Structural shape optimization—a survey. *Comput. Methods Appl. Mech. Engrg.* **57**(1), 91–106 (1986). DOI 10.1016/0045-7825(86)90072-1
- Haslinger, J., Mäkinen, R.A.E.: *Introduction to Shape Optimization. Theory, Approximation, and Computation.* SIAM, Philadelphia (2003)
- Heikkola, E., Rossi, T., , Roivanen, J.: Fast direct solution of the helmholtz equation with a perfectly matched layer or an absorbing boundary condition. *International Journal for Numerical Methods in Engineering* (2003). DOI 10.1006/jcph.1998.5979
- Ihlenburg, E.: *Finite Element Analysis of Acoustic Scattering.* Springer (1998)
- Jameson, A.: Aerodynamic design via control theory. *J. Sci. Comput.* **3**, 233–260 (1988). DOI 10.1007/BF01061285
- van Keulen, F., Haftka, R.T., Kim, N.H.: Review of options for structural design sensitivity analysis. part 1: Linear systems. *Comput. Methods Appl. Mech. Engrg.* **194**, 3213–3243 (2005). DOI 10.1016/j.cma.2005.02.002
- Laporte, E., Tallec, P.L.: *Numerical Methods in Sensitivity Analysis and Shape Optimization.* Birkhäuser (2003)
- Luo, Z., Wang, M.Y., Wang, S., Wei, P.: A level set-based parameterization method for structural shape and topology optimization. *Internat. J. Numer. Methods Engrg.* **76**(1), 1–26 (2008). DOI 10.1002/nme.2092
- Miegroet, L.V., Duysinx, P.: Stress concentration minimization of 2D filets using X-FEM and level set description. *Struct. Multidiscip. Optim.* **33**, 425–438 (2007). DOI 10.1007/s00158-006-0091-1
- Mohammadi, B., Pironneau, O.: *Applied Shape Optimization for Fluids.* Oxford University Press (2001)
- Nocedal, J., Wright, S.J.: *Numerical Optimization.* Springer (1999)
- Norato, J., Haber, R., Tortorelli, D., Bendsøe, M.P.: A geometry projection method for shape optimization. *Internat. J. Numer. Methods Engrg.* **60**, 2289–2312 (2004). DOI 10.1002/nme.1044
- Noreland, D., Udawalpola, R., Berggren, M.: A hybrid scheme for bore design optimization of a brass instrument. *J. Acoust. Soc. Amer.* **128**(3), 1391–1400 (2010). DOI 10.1121/1.3466871
- Petropoulos, P.G.: On the termination of the perfectly matched layer with local absorbing boundary conditions. *Journal of Computational Physics* pp. 665–673 (1998). DOI 10.1006/jcph.1998.5979

30. Salomon, D.: *Curves and Surfaces for Computer Graphics*. Springer, New York (2006). DOI 10.1007/0-387-28452-4
31. Sigmund, O.: On the design of compliant mechanisms using topology optimization. *Mechanics Based Designs of Structures and Machines* **25**, 493–524 (1997). DOI 10.1080/08905459708945415
32. Stolpe, M., Svanberg, K.: On the trajectories of penalization methods for topology optimization. *Structural and Multidisciplinary Optimization* **21**, 128–139 (2001)
33. Szalabaj, P.: *Contemporary Architecture and the Digital Design Process*. Arcitectoral Press (2004)
34. Udawalpola, R., Berggren, M.: Optimization of an acoustic horn with respect to efficiency and directivity. *Internat. J. Numer. Methods Engrg.* **73**(11), 1571–1606 (2007)
35. Wadbro, E., Udawalpola, R., Berggren, M.: Shape and topology optimization of an acoustic horn-lens combination. *Journal of Computational and Applied Mathematics* (2010). DOI 10.1016/j.cam.2009.08.028
36. Wang, M.Y., Wang, X., Guo, D.: A level set method for structural topology optimization. *Comput. Methods Appl. Mech. Engrg.* **192**(1–2), 227–246 (2003). DOI 10.1016/S0045-7825(02)00559-5
37. Zhang, S.: A domain embedding method for mixed boundary value problems. *C. R. Acad. Sci. Paris Sér. I Math.* **343**(4), 287–290 (2006)